The Astrophysical Journal, 959:116 (16pp), 2023 December 20 https://doi.org/10.3847/1538-4357/ad0c57

Evidence for Low-power Radio Jet–ISM Interaction at 10 pc in the Dwarf AGN Host NGC 4395

Payel Nandi[1,2], C. S. Stalin[2], D. J. Saikia[3], Rogemar A. Riffel[4], Arijit Manna[5], Sabyasachi Pal[5], O. L. Dors[6], Dominika Wylezalek[7], Vaidehi S. Paliya[3], Payaswini Saikia[8], Pratik Dabhade[9], Markus-Kissler Patig[10], and Ram Sagar[2]

[1] Joint Astronomy Programme, Department of Physics, Indian Institute of Science, Bangalore 560012, India; payel.nandi@iiap.res.in
[2] Indian Institute of Astrophysics, Block II, Koramangala, Bangalore 560034, India
[3] Inter-University Centre for Astronomy and Astrophysics (IUCAA), SPPU Campus, Pune 411007, India
[4] Departamento de Física, CCNE, Universidade Federal de Santa Maria, 97105-900, Santa Maria, RS, Brazil
[5] Midnapore City College, Kuturia, Bhadutala, Paschim Medinipur, West Bengal, 721129, India
[6] UNIVAP—Universidade do Vale do Paraíba. Av. Shishima Hifumi, 2911, CEP: 12244-000 São José dos Campos, SP, Brazil
[7] Astronomisches Rechen-Institut, Zentrum fur Astronomie der Universitat Heidelberg, Monchhofstr. 12-14, D-69120 Heidelberg, Germany
[8] Center for Astro, Particle and Planetary Physics, New York University Abu Dhabi, P.O. Box 129188, Abu Dhabi, UAE
[9] Instituto de Astrofísica de Canarias, Calle Vía Láctea, s/n, E-38205, La Laguna, Tenerife, Spain
[10] ESA—ESAC - European Space Agency, Camino Bajo del Castillo s/n, E-28692 Villafranca del Castillo, Madrid, Spain

Received 2023 June 3; revised 2023 October 26; accepted 2023 November 10; published 2023 December 13

Abstract

Black-hole-driven outflows in galaxies hosting active galactic nuclei (AGN) may interact with their interstellar medium (ISM) affecting star formation (SF). Such feedback processes, reminiscent of those seen in massive galaxies, have been reported recently in some dwarf galaxies. However, such studies have usually been on kiloparsec and larger scales and our knowledge of the smallest spatial scales to which these feedback processes can operate is unclear. Here we demonstrate radio jet−ISM interaction on the scale of an asymmetric triple radio structure of ∼10 pc size in NGC 4395. This triple radio structure is seen in the 15 GHz continuum image and the two asymmetric jet-like structures are situated on either side of the radio core that coincides with the optical Gaia position. The high-resolution radio image and the extended [O III]λ5007 emission, indicative of an outflow, are spatially coincident and are consistent with the interpretation of a low-power radio jet interacting with the ISM. Modelling of the spectral lines using `MAPPINGS`, and estimation of temperature using optical integral field spectroscopic data suggest shock ionization of the gas. The continuum emission at 237 GHz, though weak, was found to spatially coincide with the AGN. However, the CO(2−1) line emission was found to be displaced by around 20 pc northward of the AGN core. The spatial coincidence of molecular $H_2\lambda2.4085$ along the jet direction, the morphology of ionized [O III]λ5007, and displacement of the CO(2−1) emission argues for conditions less favorable for SF in the central ∼10 pc region.

Unified Astronomy Thesaurus concepts: Dwarf galaxies (416); Active galactic nuclei (16); Radio jets (1347); AGN host galaxies (2017)

1. Introduction

Active galactic nuclei (AGN), powered by the accretion of matter onto supermassive black holes at the centers of galaxies (Rees 1984), affect their host galaxies through the feedback processes. They can have an impact on the interstellar medium (ISM) of their hosts via energetic outflows (Venturi et al. 2021). These outflows, driven by radiation pressure, jets, or winds from AGN, can occur from accretion disk to galaxy scales (Mukherjee et al. 2018; Morganti et al. 2021), and can inhibit (negative feedback; Maiolino et al. 2012) or enhance star formation (SF; positive feedback; Maiolino et al. 2017; Nesvadba et al. 2020). Both positive and negative feedback processes are also seen in a single system (Shin et al. 2019; García-Bernete et al. 2021). Outflows affecting SF through the interaction of radio jets with the ISM in the host galaxies are known for large massive galaxies (for reviews, see Fabian 2012; Saikia 2022). Recent observational evidence of dwarf galaxies hosting an AGN (Schutte & Reines 2022) challenges theoretical models that generally invoke supernovae feedback in dwarf galaxies (Koudmani et al. 2022; Nandi et al. 2023). Also, recently, outflows have been observed in an AGN hosted by dwarf galaxies (Manzano-King et al. 2019; Bohn et al. 2021). Available observations of AGN have usually identified the impact of jets on the ISM on kiloparsec or larger scales. To have a clear understanding of the effect of jets on the ISM, one needs to study their impact from sub-parsec to kiloparsec and larger scales. There is hardly any observational evidence of jet −ISM interaction and its impact on the host galaxies of AGN on parsec scales.

NGC 4395 is a bulgeless dwarf galaxy at a distance of 4.3 ± 0.3 Mpc (Thim et al. 2004) and hosting a radio-quiet AGN (Filippenko & Sargent 1989). Its nucleus has the optical spectrum characteristic of a Seyfert 1.8 type AGN (Véron-Cetty & Véron 2006), hosts a black hole (Filippenko et al. 1993) in the mass range of $10^4-10^5\ M_\odot$ (Peterson et al. 2005; Woo et al. 2019), and is variable in X-ray wavelengths (Vaughan et al. 2005). NGC 4395 appeared unresolved in the Very Large Array (VLA) A-configuration image at 1.4 GHz with a flux density of 1.68 mJy (Ho & Ulvestad 2001). In this paper, we present the first observational evidence of a low-power radio jet in NGC 4395 interacting with the ISM of its

Table 1
Details of the Data Used in This Work

Telescope	Filter/Wavelength/Energy	FoV	Resolution/Synthesized Beam Size	Exposure Time
Chandra	0.5−7.0 keV	∼8′	∼1″	79 ks
HST	F507N ($\lambda_{\rm eff}$= 5009.7 Å, $\Delta\lambda$ = 66.8 Å)	∼2′.7	∼0″.1	1521 s
	F547M ($\lambda_{\rm eff}$= 5435.8 Å, $\Delta\lambda$ = 717.0 Å)	∼2″.7	∼0″.1	746 s
MaNGA	3600–10000 Å	∼30″ × 30″	∼1°5	5400 s
GMOS	4500–7300 Å	∼5″.0 × 3″.5	∼0°5	2880 s
NIFS	2.2 μm	∼3.4″ × 3.4″	∼0°2	5400 s
VLA	5 GHz	∼8′	1″.75 × 1″.19, 89°	1090 s
	15 GHz	∼3′	0″.129 × 0″.124, −18°	239 s
ALMA	237 GHz, CO(2−1)	∼19″	1″.9 × 1″.25, 3°	2037 s
	237 GHz, CO(2−1)	∼19″	0″.81 × 0″.47,356°	423 s

Note. These are all archival observations.

host galaxy, driving shocks, and ionized outflow on the parsec scale. Adopting a cosmology of $H_0 = 70\,{\rm km\,s^{-1}\,Mpc^{-1}}$, $\Omega_M = 0.7$, $\Omega_{\rm vac} = 0.3$ and a distance of 4.3 ± 0.3 Mpc (Thim et al. 2004), 1″ in NGC 4395 corresponds to 21 pc.

2. Data Reduction and Analysis

To characterize the jet−ISM interaction on the scale of parsecs, we utilized data from both ground and space-based telescopes from low-energy radio waves to high-energy X-rays. The details of the data sets used are given in Table 1.

2.1. X-Ray

We used four epochs of observations (OBSIDs: 402, 882, 5301, 5302) carried out by the Chandra X-ray observatory with the advanced CCD imaging spectrometer (ACIS, 0.5–7 keV) for exposures ranging from ∼1 to ∼31 ks. We reduced the data using the Chandra Interactive Analysis of Observations (CIAO, version 4.14) software and calibration files (CALDB version 4.9.8). We first downloaded the data and reprocessed them by running the task `chandra_repro` to generate the cleaned and calibrated event files. Next, we combined all the event files, computed the exposure maps, and generated an exposure-corrected image in the default 0.5–7 keV energy range for a total exposure of ∼79 ks. We adopted the task `merge_obs` for this purpose. We also rebinned the data by one-quarter of the native 0″.492 per pixel giving an effective resolution of 0″.123 per pixel. The image with a size of 1″ × 1″ is shown in Figure 1. The red cross in the image is the optical Gaia position.

2.2. Optical Imaging

Observations of NGC 4395 carried out by HST WFC3-UVIS2 using a range of filters are available in the Hubble Space Telescope (HST) archive[11] (Proposal ID: 12212, PI: D. Michael Crenshaw). Of these, we used the data in two filters, one F502N, which is centered at 5009.87 Å, and the other F547M, which is centered around the nearby continuum at 5756.9 Å. Our aim here is to get the [O III]λ5007 image from the observation done in the F502N filter, which in addition to the [O III]λ5007 line emission also contains the continuum emission. One of the ideal ways to remove the continuum emission from the observed F502N narrowband image is to use observations in medium-band filters both blueward and redward of the F502N filter. In such a scenario, observations in the medium-band filters that flank the narrowband filter can be used to get the continuum slope. The slope thus obtained can give us an estimate of the continuum that can be subtracted from the F502N data to get the line image. However, in the present case, we have only one medium-band filter observation, which is adjacent and redward of the F502N filter. Given this, we adopted the following to get the line image. Under the assumption that the continuum emission around [O III]λ5007 line has a zero slope (which is in agreement with spectra in this case), we selected six source-free regions having sizes of 10″ × 10″ in the F547M and F502N observations, determined the scale factors and applied the mean scale factor (c) and subtracted one filter observation from the other as given below,

$$f\,({\rm line}) = c{*}f\,(N) - f\,(M). \qquad (1)$$

Here, $f(N)$ and $f(M)$ are the brightness in counts per second in the narrow F502N filter (that contains the [O III]λ5007 emission line) and medium-band filter F547M (that contains the continuum emission). The parameter c is the scaling factor, which is the mean of the ratio of the fluxes in the narrowband filter, F502N, and the medium-band filter, F547M, determined from six source-free regions. Then we converted the observed [O III]λ5007 (continuum-subtracted) images to flux scale using

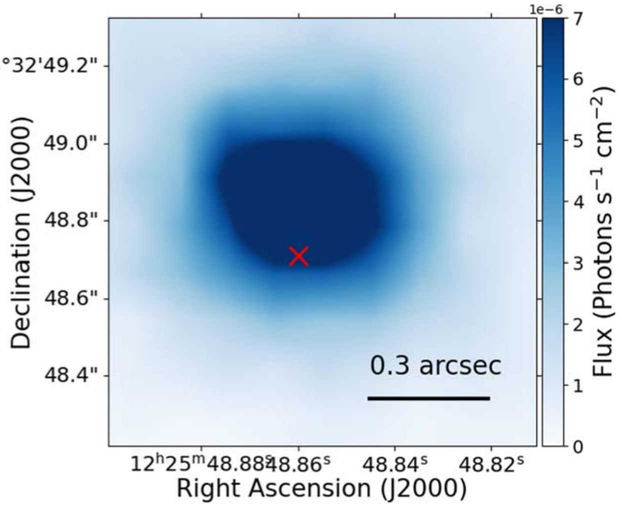

Figure 1. X-ray Image of NGC 4395 in the 0.5–7 keV energy range from Chandra. The red cross is the optical Gaia the position.

---

[11] Mikulski Archive for Space Telescopes (MAST); https://archive.stsci.edu/; the specific observations we used are available at doi:10.17909/jvzq-5d59.

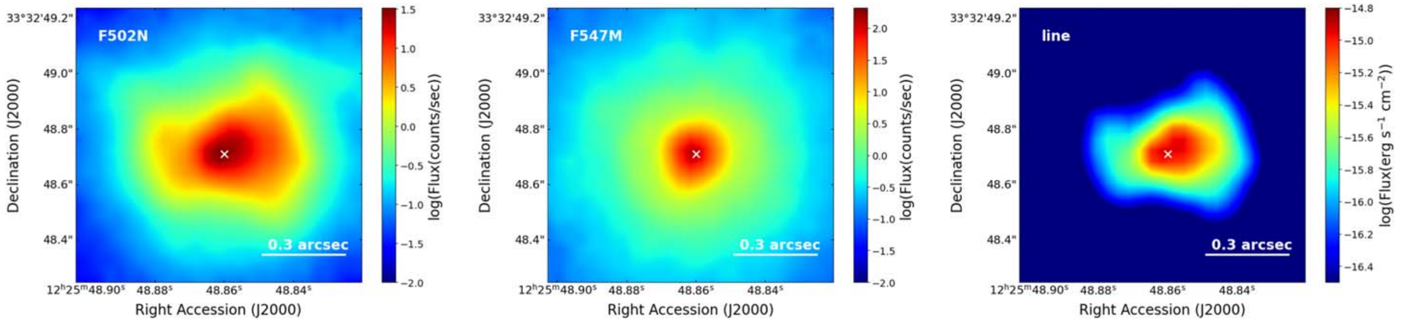

Figure 2. Left panel: the narrowband image from HST in the F502N filter that contains the emission from both the ionized [O III]λ5007 gas and the continuum. Middle panel: the continuum image from HST in the F547M filter. Right panel: difference image after subtraction of the scaled continuum F547M filter image from the narrowband F502N filter image. This difference image reveals an asymmetric biconical [O III]λ5007 outflow. The white cross in all the figures is the optical core (Gaia position).

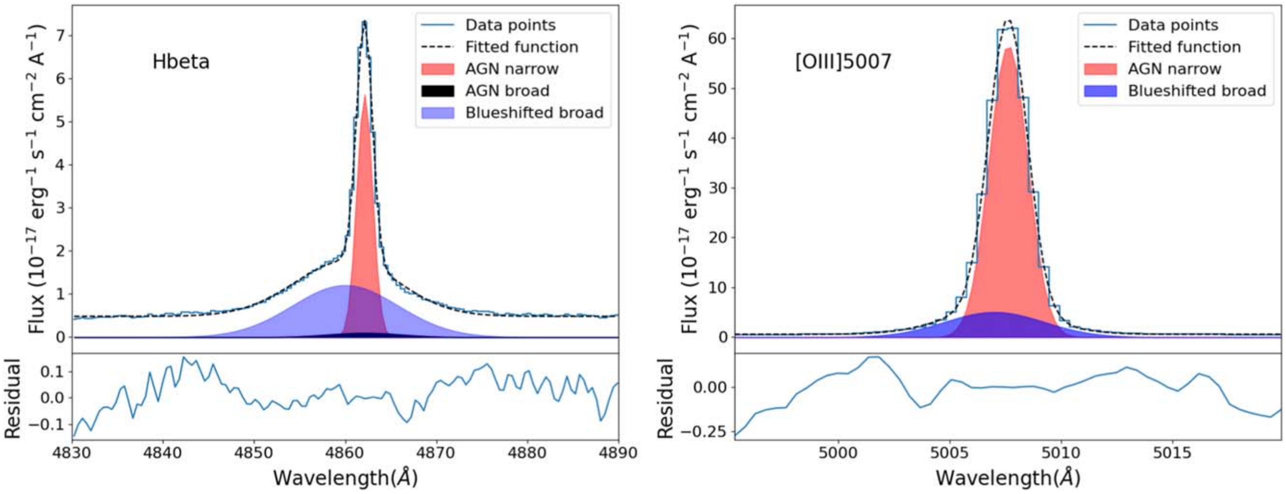

Figure 3. Gaussian fit to the observed Hβ (left) and [O III]λ5007 (right) emission lines along with the residuals (lower panel of each spectrum). Here, shaded blue is the Gaussian fit to the outflowing component, red and black are the Gaussian fits to the narrow and broad components, and the dotted black line is the best-fit spectrum. The observed spectra are shown as a solid blue line.

the KEYWORD `PHOTFLAM` given in the image headers. The observed medium-band F547M image, the narrowband F502N image, and the continuum-subtracted image are shown in Figure 2. These images have an FWHM angular resolution of $\sim 0\farcs1$.

2.3. Optical/Infrared Integral Field Spectroscopy

We used archival near-infrared and optical integral field spectroscopic (IFS) observations obtained with the Gemini and SDSS telescopes.

2.3.1. Gemini

For the optical, we used the archival data from the Gemini Multi-Object Spectrograph (GMOS) under program ID GN-2015A-DD-6 (PI: Mason Rachel). GMOS with a field of view (FoV) of $5\farcs0 \times 3\farcs5$ covers the spectral range from 4500–7300 Å. In the infrared, we used the archival data from the adaptive optics-assisted K-band observations acquired with the near-infrared integral field spectrograph (NIFS) under program ID GN-2010A-Q-38 (:PI. Anil Seth). The K band centered at 2.2 μm covers an FoV of $3\farcs4 \times 3\farcs4$. The data cubes in GMOS observations have a spatial sampling of $0\farcs05$ pixel^{-1}. The spectral resolution is 90 km s^{-1} and the angular resolution is $0\farcs5$ (Brum et al. 2019). Similarly, the data cubes in the NIFS observations have a spatial sampling of $0\farcs05$ pixel^{-1}. The spectral resolution is 45 km s^{-1} and the angular resolution is $0\farcs2$ (Brum et al. 2019). We reduced the GMOS and NIFS data following standard procedures in IRAF (see Brum et al. 2019 for details). The GMOS data is seeing limited, while NIFS data is AO assisted.

For fitting the emission lines, we followed a nonparametric approach, which involves the removal of the underlying continuum and fitting multiple Gaussian components to the emission lines. In the case of GMOS data, we identified line-free regions on either side of our region of interest, namely, the [O III]λ5007 region ($\lambda\lambda$ = 4990–5040 Å). We fitted a first-order polynomial to the line-free regions and then subtracted the function from the observations. After continuum subtraction, we fitted the [O III]λ5007 emission line with two Gaussian components to extract the flux and other properties of the line using the nonlinear least squares minimization algorithm within the `Curvefit` module of `SciPy` (Virtanen et al. 2020). An example of the fit is shown in Figure 3. For the broad Hβ line, we fitted three Gaussian components, one for the narrow AGN component, the second for the broad AGN component, and the third for the broad outflowing component. While fitting the broad and narrow AGN components we fixed the peak velocity to be the same; however, the line widths were treated as free parameters and were allowed to vary. For the broad outflowing component, no restriction was imposed, either for the peak of

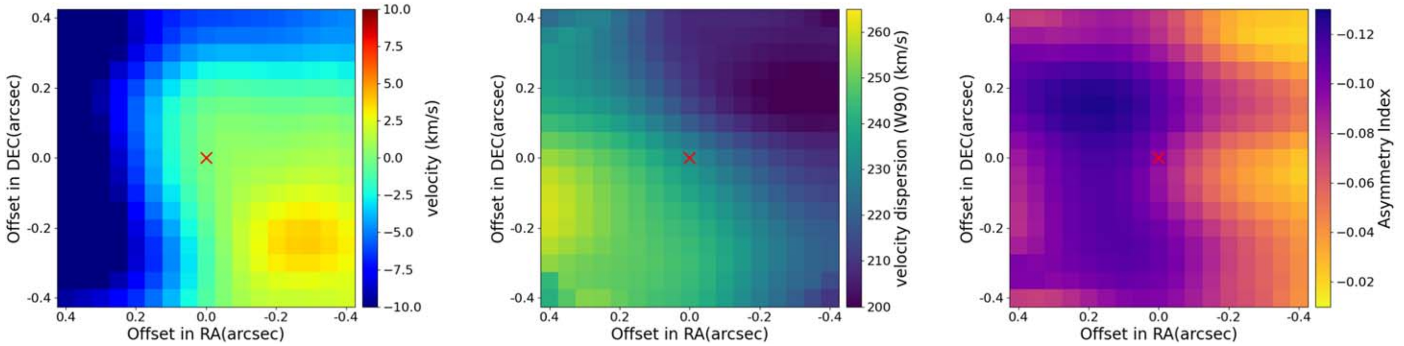

Figure 4. Kinematics map of [O III]λ5007 line emission. Left panel: velocity map. Middle panel: map of the W90 parameter, which is equivalent to velocity dispersion. Right panel: map of asymmetry index. The red cross represents the core (optical Gaia position).

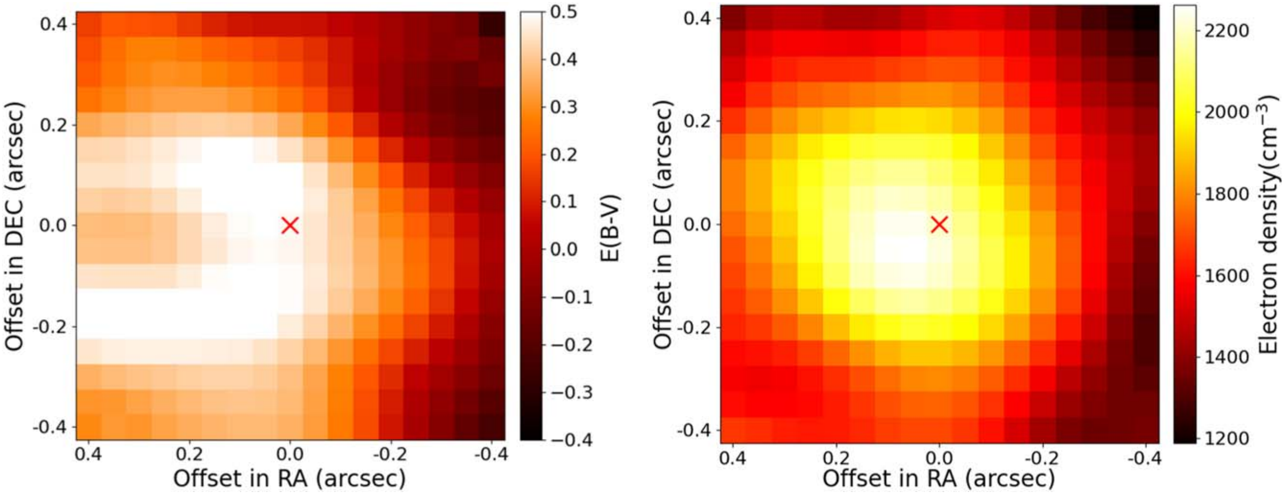

Figure 5. Left panel: extinction *E(B−V)* map. Right panel: map of electron density calculated from the [S II]$\lambda\lambda$ 6717,6731 line ratio. The red cross is the core (optical Gaia position).

the component or the width of the component. From our fits to the Hβ line, we obtained a σ of 385 km s^{-1} for the broad Hβ component, which is similar to the value of $\sigma = 334$ km s^{-1} obtained by Brum et al. (2019). The procedure adopted in this work to fit the emission lines is thus appropriate. We fitted the lines [N II]$\lambda\lambda$ 6548,6584 and Hα lines together. For the Hα line, we used three Gaussian components similar to that used for the Hβ line. In addition, we used two Gaussians for the two [N II]$\lambda\lambda$ 6548,6584 lines. Here, we tied the widths of the [N II] $\lambda\lambda$ 6548,6584 lines to the width of the narrow component of Hα. For the narrow lines such as [N II]λ5755, [S II]$\lambda\lambda$ 6716,6732, and the H2λ2.4085 line from NIFS, we followed the same methodology used for the [O III]λ5007 line.

From the Gaussian fits to the [O III]λ5007 line emission in the observed spectra (not corrected for instrumental resolution), we estimated nonparametric values (Zakamska & Greene 2014) such as the velocity ($v50$, the velocity where the cumulative flux of the line becomes half of the total flux), velocity dispersion ($\mathrm{W90} = v95 - v5$, where $v95$ and $v5$ are the velocities at which the flux becomes 95% and 5% of total flux), and the asymmetry $\left(R = \frac{(v95 - v50) - (v50 - v5)}{v95 - v5}\right)$ of the line. Also, from fits to the [S II] doublet and using the ratio of the [S II]λ6716 to [S II]λ6731 lines, we estimated the electron density. This line ratio is sensitive to electron densities of the order of $\sim 10^2$–10^4 cm^{-3}. For estimating the electron density, we assumed an electron temperature of 10,000 K. We calculated the internal extinction $E(B-V)$ from the Hα and Hβ line ratio using the following formula (Miller & Mathews 1972; Veilleux et al. 1995):

$$E(B - V) = 1.925 \times \log \frac{\left(\frac{I_{\mathrm{H}\alpha}}{I_{\mathrm{H}\beta}}\right)_{\mathrm{obs}}}{3.1}. \tag{2}$$

The maps for the velocity and velocity dispersion of the [O III] λ5007 line-emitting gas and for the asymmetry parameter of the line are given in Figure 4, whereas the *E(B-V)* map and the electron density map are shown in Figure 5. The molecular $\mathrm{H}_2\lambda$2.4085 image is shown in Figure 6. These figures cover approximately central $1'' \times 1''$ region of NGC 4395. This is because the radio emission at 15 GHz has an extension of $\sim 0\farcs5$ and our aim is to investigate the interaction of the radio jet with the ISM.

2.3.2. SDSS/MaNGA

From the Sloan Digital Sky Survey (SDSS) we used data of NGC 4395 observed as part of the Mapping Nearby Galaxies at Apache Point Observatory (MaNGA) survey. The pixel scale of the MaNGA product is $0\farcs5 \times 0\farcs5$. It covers the wavelength range of 3600–10000 Å with a spectral resolution ($\lambda/\Delta\lambda$) of $\approx$2000. We used the spectrum of the central brightest pixel, which covers the central $0\farcs5 \times 0\farcs5$ region of NGC 4395, and

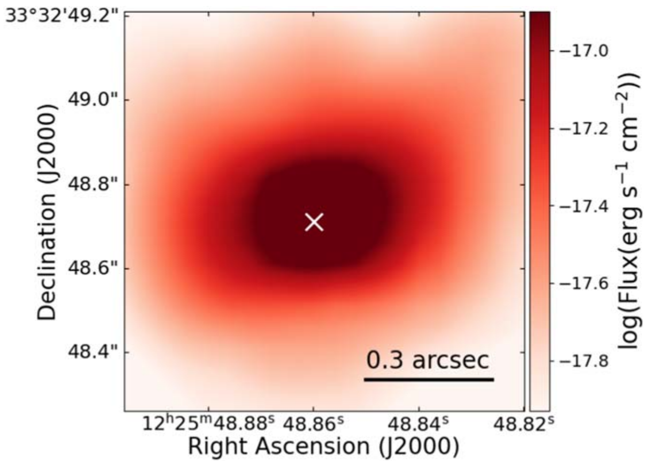

Figure 6. The molecular $H_2\lambda2.4085$ image of NGC 4395. The core of NGC 4395 taken as the optical Gaia position is shown as a white cross.

largely encompasses the ∼0.″5 extent (total) of the radio jet, the region of interest in this paper to investigate the radio jet−ISM interaction. By using the advantage of this wavelength region, we detected shock-sensitive lines [O III]λ4363, He IIλ4886 (which are beyond the limit of GMOS), [O III]$\lambda\lambda$ 4959,5007, Hβ, [N II]λ5755, and [N II]$\lambda\lambda$ 6548,6584 lines (as shown in Figure 7) and estimated the parameters. These parameters are thus a representation of the physical conditions in the central 0.″5 × 0.″5 region. We fitted the emission lines in the same way as explained in Section 2.3.1 and estimated the emission line fluxes.

2.4. ALMA

We used the archival data, observed with the high-resolution Atacama Large Millimeter/submillimeter Array (ALMA) with 12 m antennas (Data ID: 2017.1.00572.S, PI: Davis, Timothy). The observations were carried out on 2018 March 22, and 2019 January 23, with ALMA band 6 in the frequency range of 227.47–246.43 GHz. The on-source integration time was 2037 and 423 s, respectively. During the observations, a total of 46 antennas were used, with a minimum baseline of 15.1 m and a maximum baseline of 783.5 m. For the observations on both days, the quasar J1221 + 2813 was observed as a phase calibrator, and J1229 + 0203 was observed as a flux density and bandpass calibrator.

We reduced the data using the Common Astronomy Software Application (CASA v5.4.1) with the standard data reduction pipeline of the ALMA observatory. We show in Figure 8 (upper left) the continuum image of NGC 4395 at 237.1227 GHz observed on 2018 March 22 having a synthesized beam size of 0.″805 × 0.″469 along a position angle (PA) of 356°. From two-dimensional Gaussian fits we found the peak and integrated flux densities to be 93 ± 20 μJy beam^{-1} and 131 ± 45 μJy respectively. Also, the continuum image at 237.1227 GHz, observed on 2019 January 23 is shown in Figure 8 (upper right). It has a synthesized beam size of 1.″935 × 1.″253 along PA of 3°. From Gaussian fits to the data, we found the peak and integrated flux densities to be 274 ± 21 μJy beam^{-1} and 287 ± 41 μJy, respectively. These results from an independent analysis are also in agreement with those of Yang et al. (2022). We used the task `TCLEAN` to generate the spectral data cubes. The CO line maps are shown in Figure 8 (lower panels). From both observations, we found the peak of the CO(2−1) emission to be displaced by around 0.″9 (∼20 pc) from the nucleus (as determined by Gaia) of NGC 4395.

2.5. VLA

The source was observed with the VLA A configuration at 15 GHz (PI: Payaswini Saikia, Legacy ID: AS1409). We reduced the data using standard procedures that include flagging bad data using CASA (see Saikia et al. 2018 for details). The beam size obtained is 0.″129 × 0.″124 with a PA of −18°. The final image at 15 GHz has an rms noise of 11 μJy beam^{-1}. The contours of the 15 GHz image shown in the left panel of Figure 9 are at 0.03, 0.05, and 0.10 mJy beam^{-1}. The western jet component has a peak flux density of 44.6 ± 1.0 μJy beam^{-1}. Though it is fainter related to the core and eastern components, it is detected at about the 4σ level.

The source was also observed at 4.8 GHz (C band) in the VLA B-configuration (PI: J.S. Ulvestad, Legacy ID: AU079). We reduced this data using standard procedures in AIPS by using 3C286 as the flux density calibrator and 1227 + 365 as a phase calibrator. We achieved an rms noise of 48 μJy beam^{-1}. The beam size in the final reduced image is 1.″75 × 1.″19 along a PA of 89°. The final images at 15 and 4.8 GHz are shown in Figure 9.

3. Results and Discussion

3.1. Radio Morphology

The VLA 15 GHz image (Figure 9, left panel) showed the source to be a triple with E being the eastern component of the triple (Saikia et al. 2018). The weaker central component of the triple is coincident with the optical Gaia position, while component E is displaced from it by about 220 mas, corresponding to a projected distance of 4.6 pc. The western component (W) is separated from the central component by 4.2 pc. However, the overall projected extension of the source is ∼10 pc. The source is also highly asymmetric in brightness, the ratio of peak brightness of components E to W is 3.8. Component E has a spectral index, α, of −0.64 ± 0.05 ($S \propto \nu^{\alpha}$) and a brightness temperature, T_B of $(2.3 \pm 0.4) \times 10^6$ K, showing it to be a nonthermal source. For the central feature $\alpha = -0.12 \pm 0.08$, and non-detection of a sub-parsec-scale compact component sets $T_B < 5.9 \times 10^5$ K (Yang et al. 2022). Radio cores being resolved out in low-mass AGN when observed with milliarcsec resolution has been reported earlier (Nyland et al. 2017). Variability or episodic nuclear jet activity could also contribute to the non-detection of a core.

The triple structure is strongly reminiscent of bipolar jet ejection in radio-loud AGN, and we suggest that the outer components (W and E) are formed by weak radio jets from the intermediate-mass black hole, and refer to the central component as the radio core. We refer to W and E, the endpoints of the radio emission as jets in this paper to explore jet−ISM interaction. Low-power radio jets ($P < 10^{42}$ erg s^{-1}) can have a significant effect on the ISM of the host galaxy, interacting with clouds of gas and heating the gas, entraining ambient gas, losing collimation, and sometimes forming arc-like fronts (Rampadarath et al. 2018).

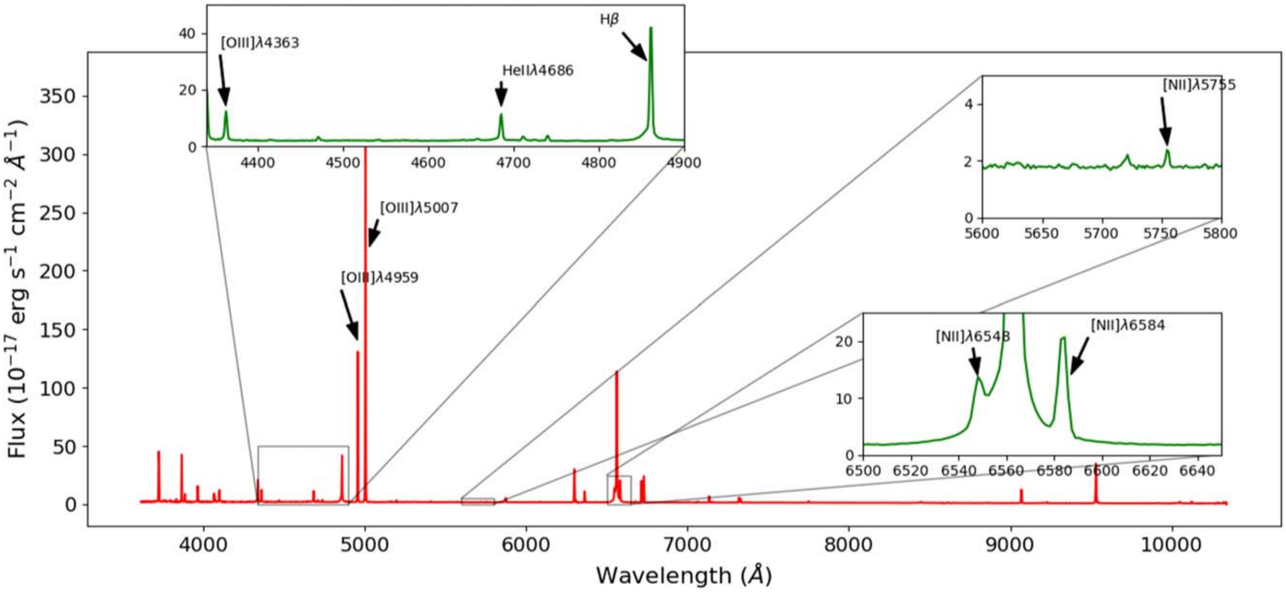

Figure 7. The rest-frame spectrum of NGC 4395 from MaNGA covering the central brightest $0\farcs5 \times 0\farcs5$. The lines used to calculate the line intensity ratios are marked.

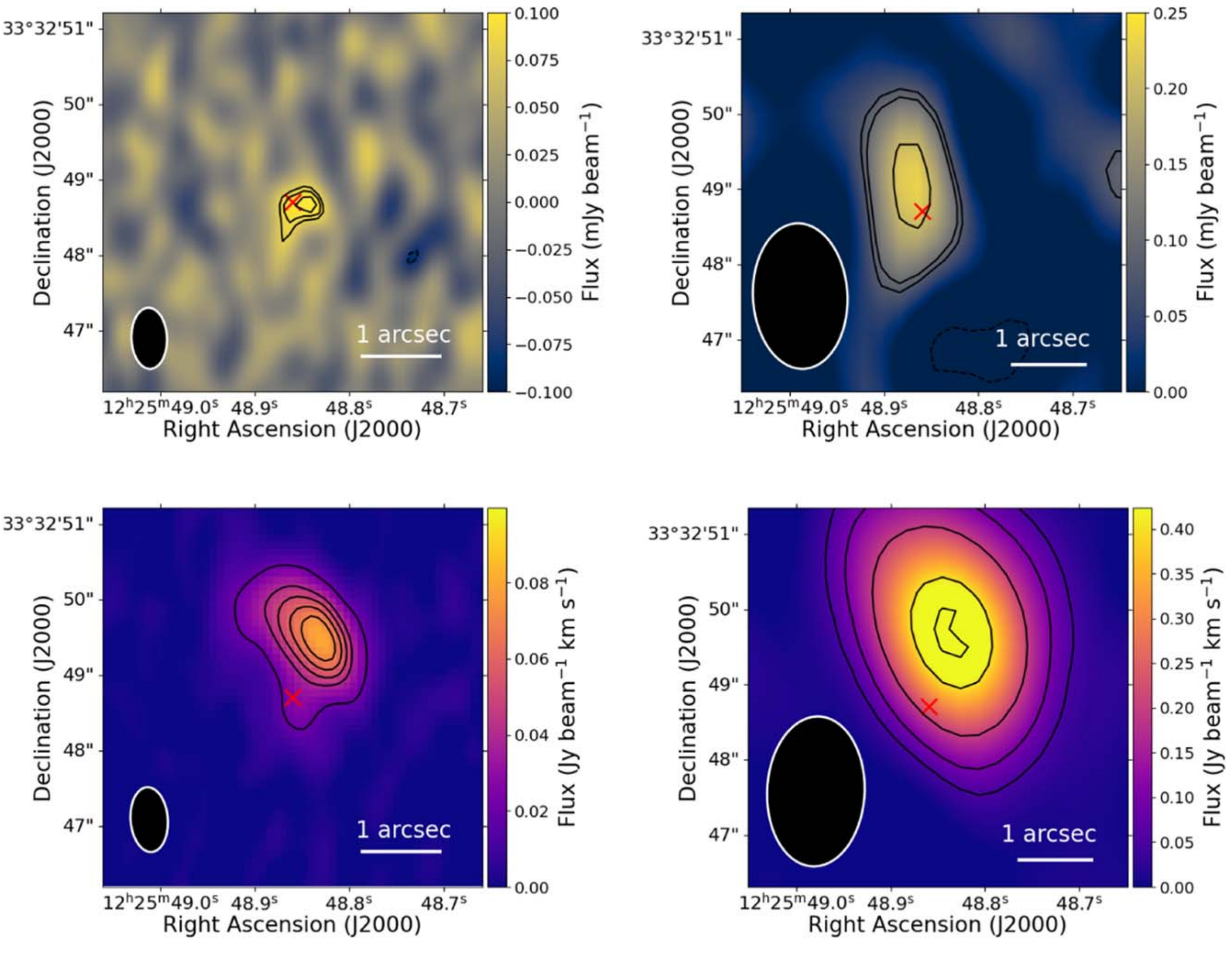

Figure 8. Upper panel: the continuum emission at 237 GHz based on observations with ALMA on 2018 March 22 (left) and 2019 January 23 (right). The contours are -0.08, 0.08, 0.09, and 0.1 Jy beam^{-1} (left) and −0.08, 0.08, 0.1, and 0.2 Jy beam^{-1} (right). Lower panel: the CO(2−1) emission for the observation on 2018 March 22 (left) and 2019 January 23 (right). The contours are 0.02, 0.04, 0.05, 0.06, and 0.07 Jy beam^{-1} km s^{-1} (left) and 0.05, 0.1, 0.2, 0.4, and 0.5 Jy beam^{-1} km s^{-1} (right). The red cross is the optical Gaia position. The synthesized beams are shown by black ellipses.

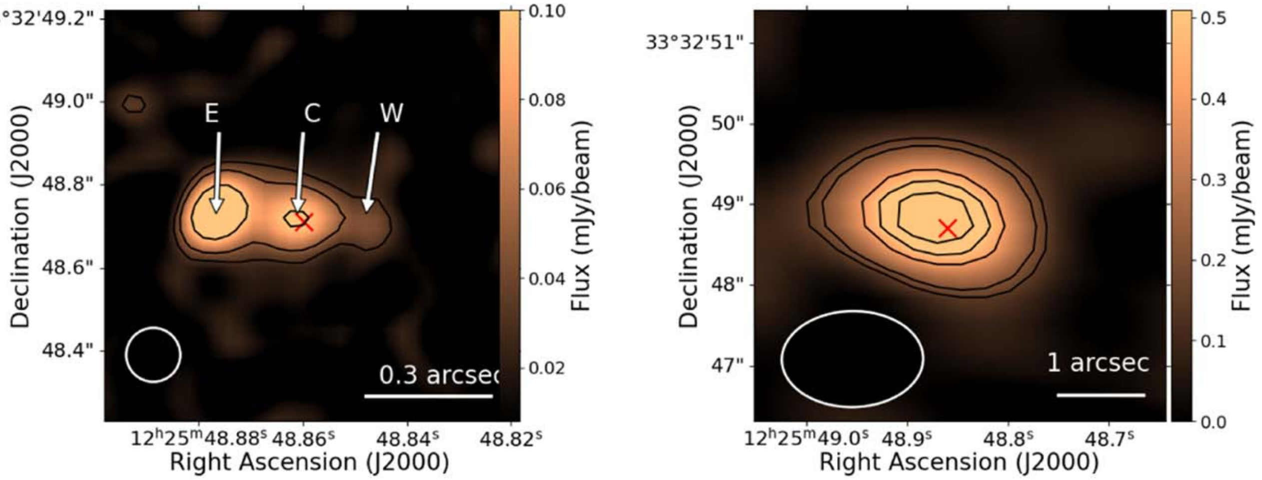

Figure 9. Left: the VLA radio images at 15 GHz with a size of 1″ × 1″. The contours are at 0.03, 0.05, and 0.10 mJy beam^{-1}. The rms noise is 11 μJy beam^{-1}. Here, C is the radio core, E is the eastern jet component and W is the western jet component. Right: the 4.8 GHz VLA image with a size of 5″ × 5″. The contours are at 0.15, 0.20, 0.40, 0.50, and 0.60 mJy beam^{-1}. The rms noise is 48 μJy beam^{-1}. The synthesized beams are shown as white ellipses. These have a size of 0.″129 × 0.″124 with a PA of −18° (left panel) and 1.″75 × 1.″19 with a PA of 89° (right panel). The red cross in both panels represents the optical Gaia position.

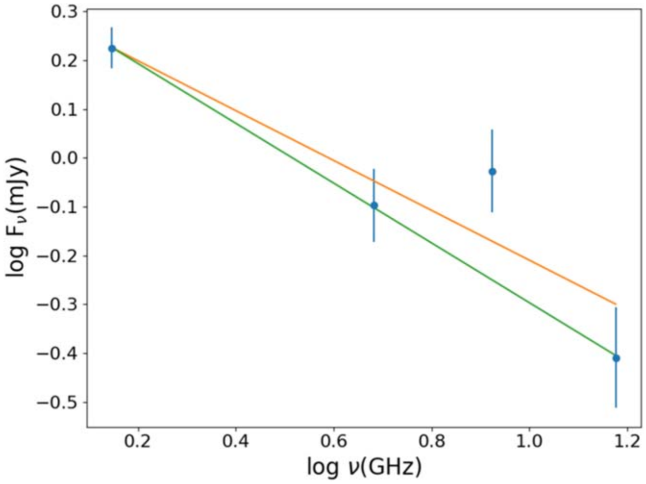

Figure 10. Plot of flux density against frequency. The solid lines are linear least squares fits to the data. The orange line is the fit to all the data points, while the green line is the fit excluding the 8.4 GHz measurement.

3.2. Nature of Radio Emission in the Central 10 pc Region

The radio emission observed in the central parsec-scale region of a dwarf galaxy could be from a variety of physical processes, such as low-power jets, AGN-driven wind, SF, coronal activity, and free–free emission from thermal gas (Panessa et al. 2019). Radio structure, spectral index, polarization characteristics of the radio emission if detectable in the future, spatial correlation of radio structure and different gaseous components, and spectral line diagnostics of the different components of the ISM could provide valuable clues in identifying the dominant processes. In NGC 4395, the radio morphology of a triple radio source clearly shows signs of interaction on the eastern side, which appears to bend sharply, as seen in the high-resolution image (see Yang et al. 2022), indicating jet–ISM interaction. This was reinforced by a detailed study of the line-emitting gas. The [O III]λ5007 emission appears closely associated with the radio source, ionized by shocks as the jets flow outward. Line-ratio diagnostics, estimation of gas temperatures from line ratios, and comparison of line ratios with theoretical predictions using `MAPPINGS` models, all showed shocks to be the dominant process responsible for the ionization. The eastern component, which is more prominent at radio wavelengths, showed stronger signs of interaction with the ISM than the western component.

The spectral index (inclusive of all the three components) derived over the 1.4−15 GHz range (see Figure 10) gives a value of $\alpha = -0.51 \pm 0.11$ ($S_\nu \propto \nu^\alpha$) and $\alpha = -0.61 \pm 0.01$ excluding the 8.4 GHz point. We note here that the flux density measurements are not simultaneous and could be affected by the variability of the central AGN. However, considering only the eastern jet/component, Yang et al. (2022) obtained a value of $\alpha = -0.64 \pm 0.05$. This is very close to the theoretical injection spectral index (Kirk et al. 2000). Considering the source to have a spectral index in the range of −0.51 to −0.64, the inverse Compton scattering of the cosmic microwave background photons and radio photons can give rise to a power-law X-ray spectrum whose photon index, Γ, can be 1.51–1.64. This is close to the value of $\Gamma = 1.67$ found by Kammoun et al. (2019) from an analysis of XMM data in the 2–10 keV band.

Using the observed luminosity at 1.4 GHz, we calculated the jet power as (Cavagnolo et al. 2010)

$$P_{\rm jet} = 5.8 \times 10^{43}\left(\frac{L_{\rm 1.4GHz}}{10^{40}{\rm erg\ s^{-1}}}\right)^{0.7}. \tag{3}$$

Using $L_{\rm 1.4GHz} = (6.1 \pm 0.3) \times 10^{34}$ erg s^{-1} (Ho & Ulvestad 2001) we estimated the jet power to be $P_{\rm jet}$=$(1.3 \pm 0.3) \times 10^{40}$ erg s^{-1}. It is thus evident that the jet in NGC 4395 is weak compared to powerful radio galaxies having typical jet powers of 10^{44}–10^{45} erg s^{-1} (Rusinek et al. 2016).

The above considerations all show that the radio emission in the central 10 pc region in NGC 4395 is from a low-power jet launched by an intermediate-mass black hole.

3.3. Radio And [O III]λ5007 Emission

Figure 11 shows the [O III]λ5007 map of NGC 4395 over a region of 1″ × 1″ in the total line emission (left panel), the narrow line component (middle panel), and the broad outflowing line component (right panel). Also, overplotted in these figures are the 15 GHz radio contours in green and the [O III]λ5007 HST

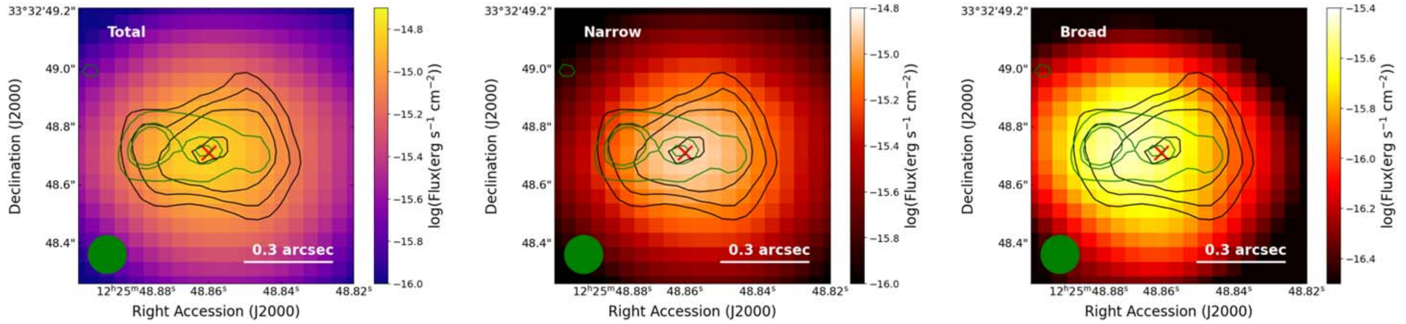

Figure 11. GMOS [O III]λ5007 image in color scale along with the radio emission at 15 GHz (green contours) with contour levels of 0.03, 0.08, and 0.1 mJy beam^{-1} and HST [O III]λ5007 emission (black contours) with contour levels of (0.05, 0.1, 0.2, 1.0) $\times 10^{-15}$ erg s^{-1} cm^{-2}. The left panel shows the GMOS total flux in [O III] λ5007, the middle panel shows the GMOS flux in the narrow component of [O III]λ5007 and the right-hand panel shows the GMOS flux in the broad component of [O III]λ5007. The red cross is the core (optical Gaia position). The green circle is the synthesized beam of 15 GHz data with a size of 0.″129 × 0.″124 along PA −18°.

emission in black. The broad outflowing component of [O III] λ5007 emission is brighter on the eastern side, where the radio emission also tends to be brighter. From these figures, it is evident that the total [O III]λ5007 emission is prevalent over the entire extent of the radio emission, with the peak of the total [O III]λ5007 emission coinciding with the peak of the central 15 GHz emission and the outflowing component of the [O III] line emission is displaced toward the east and overlaps with the eastern radio component. We note here that the peak of the [O III] λ5007 flux from GMOS and that from HST are comparable, with values of $(1.56 \pm 0.08) \times 10^{-15}$ and $(1.25 \pm 0.06) \times 10^{-15}$ erg s^{-1} cm^{-2}, respectively. The pixel scales of the [O III]λ5007 images from GMOS and HST are 0.″05 and 0.″04, respectively. The HST [O III]λ5007 emission is asymmetric and has a cone-like structure with a convex shape near the terminal points of the radio jet, resembling bow shocks in FR II radio galaxies (Kaiser & Alexander 1999). The eastern [O III]λ5007 cone has a narrower opening angle, while the western cone has a wider opening angle. Also, the western [O III]λ5007 cone has a more pronounced convex-shaped morphology compared with the eastern one. The asymmetry in the [O III]λ5007 emission could be due to the jets passing through an inhomogeneous medium. The eastern jet is brighter in the radio band, traveling in a denser and larger *E(B−V)* medium (see Figure 5), which could have ionized the gas, leading to dimmer[O III]λ5007 emission and brighter synchrotron emission because of shock-induced compression. Similarly, the western jet is traveling in a less dense medium, with smaller *E(B−V)* values and enhanced [O III]λ5007 emission. The observed morphology of the source in radio and [O III]λ5007 is unambiguous evidence for the interaction of the radio jets with the ISM of the host of NGC 4395 and is the first structural evidence of jet−ISM interaction operating on scales ∼10 pc in a triple radio source.

3.4. Multiwavelength Structure of NGC 4395

The 15 GHz image (Figure 9) shows the highly asymmetric triple structure discussed earlier. In luminous radio galaxies, the components seen on the side of the jets that interact with a dense cloud in the ISM are usually nearer and brighter (Saikia et al. 2003; O'Dea & Saikia 2021), as there is greater dissipation of energy on this side and the dense clouds inhibit the advancement of the jets. In the case of NGC 4395, the brighter component is farther from the nucleus, although its high-resolution radio structure and our optical emission line study suggest the interaction of the jet with the ISM. Therefore, a degree of intrinsic asymmetry in the radio jets cannot be ruled out. The velocities of the jets in these low-luminosity AGN are small so that relativistic beaming effects are not expected to be important, as also seen in the case of Seyfert galaxies (e.g., Roy et al. 2000; Whittle et al. 2004; Lal et al. 2011).

Figure 2 shows the [O III]λ5007 image of the 1″ × 1″ from HST. We found the [O III]λ5007 emission to be prevalent over the central 1″ × 1″. The central component of the 15 GHz radio emission and the peak of the [O III]λ5007 image from HST, coincides with the optical Gaia position. The Gaia position is thus the AGN core. The right-hand panel of Figure 2 clearly shows that the [O III] gas distribution is asymmetric around the optical Gaia position (the AGN core). Also, the [O III] emission exhibits a convex-shaped morphology at the terminal points on either side of the AGN core, though less conspicuous on the eastern side, but more prominent on the western side where the radio emission is weaker. These features suggest that the structure seen in [O III] line emission could be an ionized outflow, which we explore later. A similar conclusion was also arrived at by Woo et al. (2019).

In Figure 6 we show the 1″ × 1″ map of the source in molecular H_2 at 2.4085 μm, obtained from NIFS on the Gemini telescope. The molecular H2λ2.4085 is also extended, in the east–west direction and spatially coincident with the 15 GHz radio emission. The 4.8 GHz emission (Figure 9, right panel) is also spatially coincident with the 15 GHz emission and oriented in the east–west direction. The continuum emission at 237 GHz too (the top panels in Figure 8) coincides with the central radio source at 15 GHz and the optical Gaia position. However, the CO(2−1) line emission is concentrated at a larger distance (∼0.″9) from the central nuclear emission (see Figure 8). The X-ray image (Figure 1) also shows emission centered around the nuclear region with extended emission along the east–west direction.

3.5. BPT Analysis

Emission line ratios in the optical are an essential tool to distinguish between star-forming galaxies and AGN. Also, they can be used to disentangle processes that lead to the line emission from SF, AGN, and shocks. To measure the emission line fluxes, we fitted line profiles of Hα and [N II]$\lambda\lambda$ 6548,6584, [S II]$\lambda\lambda$ 6717,6731, [O III]λ5007, and Hβ in the spectra of each spaxel, using two Gaussian components for narrow lines and three Gaussian components for the broad Balmer lines Hα and Hβ (see Section 2.3.1). The extra

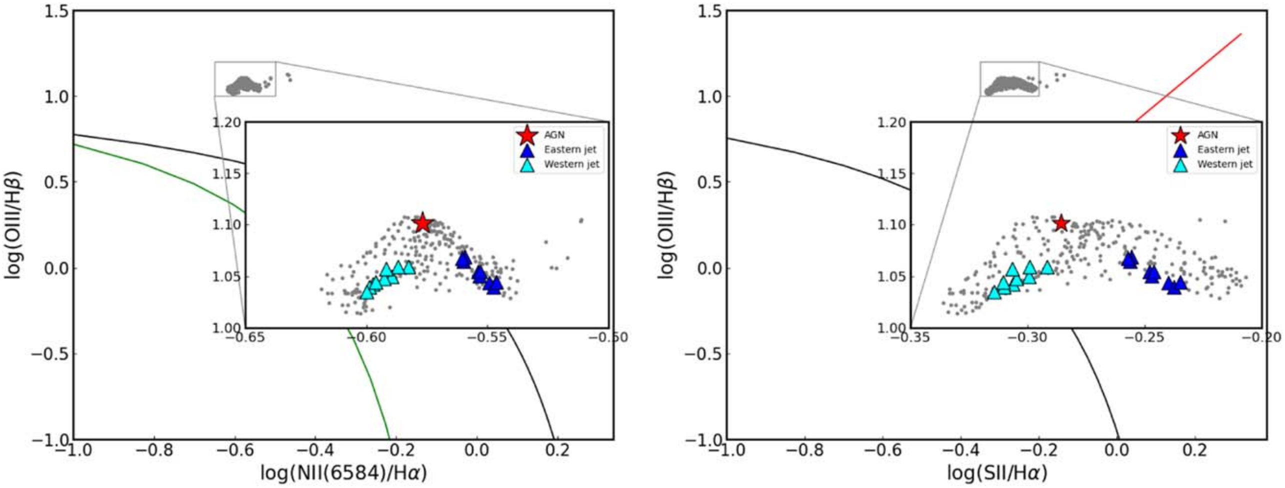

Figure 12. The position of the spaxels belonging to the central 1″ × 1″ region of NGC 4395 in the line-ratio diagnostic diagrams. The green solid curve is from Kauffmann et al. (2003), black and red solid lines are from Kewley et al. (2001). The typical error in these plots is 0.01 dex in both axes.

component in all lines represents the contribution from outflowing gas, while other components are for the broad-line region (BLR) and narrow-line region (NLR). During the fitting of the [N II] and Hα lines, the line widths of the narrow components were tied together, and the peak fluxes were left free. For Balmer lines (Hα and Hβ) we used the same velocity shift for the narrow component and one broad component, which are responsible for the NLR and BLR regions, respectively. While fitting the [S II] lines, the width of these two lines was tied together. We used the [O III]λ5007/Hβ versus [S II]/Hα as well as [O III]λ5007/Hβ versus [N II]/Hα diagnostic diagrams to investigate the physical processes causing the emission lines. These diagnostic diagrams are shown in Figure 12. Each point in these diagrams represents one spaxel in the 1″ × 1″ region centered around NGC 4395. Here, the red star is the AGN, and the blue and cyan triangles represent the spaxels in the eastern and western jet components. Though all the spaxels lie in the AGN region of the Baldwin–Phillips–Terlevich (BPT; Baldwin et al. 1981) diagram, there is a clear segregation between the core, the eastern, and the western components.

3.6. Diagnostics of the Emission Lines: Photoionization by AGN and/or Shock

3.6.1. Photoionization Modeling

To characterize the ionization processes that operate in the central 1″ region of NGC 4395, we carried out a comparison of emission line measurements from the observed GMOS spectra with photoionization and shock models from `MAPPINGS III` (Sutherland et al. 2013) and implemented in `ITERA` (Groves & Allen 2013). The emission lines in the spectra of material photoionized by AGN depend on the ionization parameter U, the slope of the ionizing continuum, β ($\phi_\nu \propto \nu^\beta$), the gas density, and its metallicity. We generated output spectra for a range of input parameters with β ranging from −2 to −1.2 and log (U) varying from −4.0 to 0.0. We assumed solar metallicity (Cedrés & Cepa 2002) and a hydrogen density of $n_{\rm H}$ = 1000 cm^{-3}.

Similarly, to generate the emission line spectra from shocked material, we used the `MAPPINGS III` code again implemented in `ITERA`. We considered shock velocities (v) between 100 and 1000 km s^{-1}. The metallicity was assumed as solar consistent with that available in the literature (Cedrés & Cepa 2002), and we considered both pure shock and shock plus precursor models. The magnetic parameter B was allowed to vary between 0.01 and 1000 μG. We show in Figure 13, the comparison between model line ratios and observed line ratios in the log([O III]λ5007/Hβ) and log([S II]/Hα) plane for photoionization by AGN (left panel) and photoionization by shocks (right panel). The observed line ratios of the spaxels in the central 1″ × 1″ tend to lie in the region predicted by shock models. Thus, the observations analyzed in this work show evidence of shocks contributing to the ionization of the gas in the central region of NGC 4395. This is possible with the hypothesis that the expanding radio jets from the central core, upon its interaction with the ISM, lead to shocks in the medium, which dominate the ionization of the gas over other processes, such as photoionization by AGN.

3.6.2. Electron Temperature Distribution

Knowledge of the electron temperature (T_e) in the central regions of AGN can help one to constrain the contribution of AGN to gas ionization. Shocks from AGN outflows could produce higher values of T_e (Riffel et al. 2021). We calculated the integrated T_e using two line intensity ratios, namely, $R_{\rm O3}$=([O III]$\lambda\lambda$ 4959,5007)/λ4363 and $R_{\rm N2}$=([N II]$\lambda\lambda$ 6548,6584)/λ5755 from MaNGA spectra and adopting the following relations (Riffel et al. 2021; Dors et al. 2020; Hägele et al. 2008):

$$\frac{T_{e[\rm O\,III]}}{10^4 K} = 0.8254 - 0.0002415 R_{\rm O3} + \frac{47.77}{R_{\rm O3}}, \quad (4)$$

$$\frac{T_{e[\rm N\,II]}}{10^4 K} = 0.537 + 0.000253 \times R_{\rm N2} + \frac{42.13}{R_{\rm N2}}. \quad (5)$$

We found $T_{e[\rm N\,II]}$=(16.4 ± 1.3) × 10^3 K and $T_{e[\rm O\,III]}$ = (16.8 ± 1.0) × 10^3 K, which are comparable within the errors. These values are too large to be produced solely by AGN photoionization (see Figure 15).

To better characterize the spatial nature of T_e, we used [N II] lines from GMOS spectra to generate a spatially resolved map of T_e. Since [O III]λ4363 is not covered by the GMOS spectra we used the line ratio $R_{\rm N2}$ to generate the T_e map. For this, we

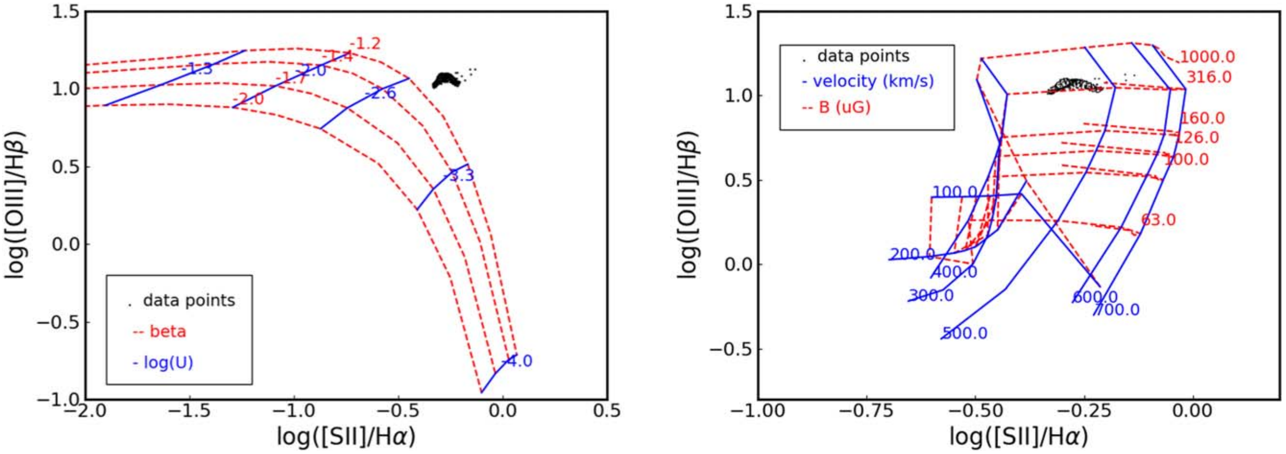

Figure 13. Comparison between predictions of the line ratios due to photoionization by AGN (left panel) and shocks (right panel) and the observed line ratios. The clustered black points are the observed data points in central 1″ × 1″. The model grids are shown for different shock velocities, magnetic fields, and ionization parameters. The typical error of the data points in these plots is 0.01 dex in both axes.

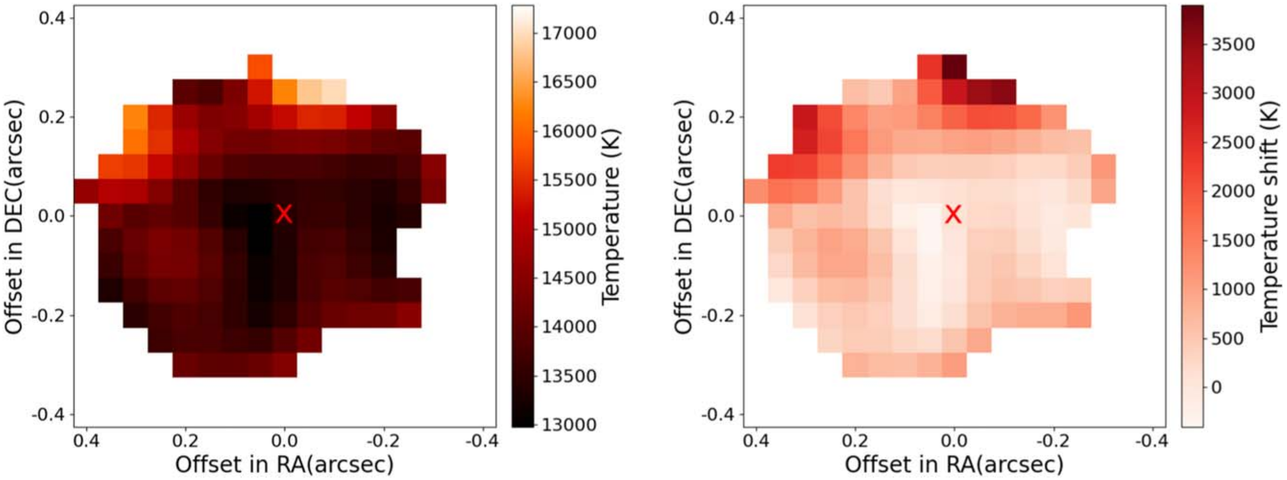

Figure 14. Left panel: temperature map from [N II] line ratio. Right panel: temperature difference map with respect to the central spaxel. The red cross is the optical Gaia position.

considered only those spaxels where the signal-to-noise ratio (ratio of the peak of the [N II]λ5755 line to the standard deviation of the pixels in the adjacent continuum) is greater than 30. The T_e map is shown in Figure 14. We found T_e to have a range of values, with the value increasing from the center of NGC 4395 outward, both toward the eastern and western terminal points of the radio jet. This increase in temperature toward the eastern and western sides is evident in the temperature difference map shown in the right panel of Figure 14. This temperature difference map is generated by subtracting each temperature value from the temperature calculated over the central $0\farcs05 \times 0\farcs05$ region. This difference in temperature is significant, as the error in the temperature estimated using Equations (3) and (5) is typically around 6%–8%. The increase in temperature from the center of NGC 4395 toward the edges (the difference in temperature is larger than the error in the estimated temperature) coinciding with the radio jet, points to the gas being mostly ionized by shocks. Shocks could be produced by the interaction of the radio jet with the ISM, and this increase of T_e from the center toward the edges is direct evidence of shock ionization (Riffel et al. 2021).

3.7. *Warm Ionized Gas and Shock*

The availability of gas reservoirs in the few tens of parsecs in the central regions of AGN is an important ingredient in the feeding and feedback processes in them. In particular, the presence of ionized gas in the central regions of AGN is believed to be a consequence of SF as well as AGN activity. Such ionized emission could also be produced by shock excitation. The presence of such ionized gas is easily traced in the optical through emission lines and could trace the effect of AGN and the presence of outflows. From recent IFU observations in the optical and infrared of the central 1″ × 1″ region of NGC 4395, Brum et al. (2019) suggest that these may be ionized by the AGN based on the location of these spatially resolved measurements in the BPT diagram (Baldwin et al. 1981) (in the case of optical) and IR line ratio diagram (in the case of infrared). However, in the zoomed-in version of the BPT diagram, the eastern component, the core, and the western component nicely become segregated (see Figure 12). It is thus likely (similar to that seen in a nearby AGN NGC 1068 by D'Agostino et al. 2019b) that the emission in the spaxels within the central 1″ × 1″ region of NGC 4395 could have contributions from AGN, besides shock ionization as discussed earlier.

Outflows can have multiple constituents, such as the hot ionized gas produced at the shock front as well as neutral and molecular gas entrained in the flow. Shocks produced by AGN-driven outflows and/or radio jet–ISM interaction could also provide the possibility of energetic feedback altering the SF characteristics of the ISM. We consider here the possibility of the shocks leading to the observed morphology of the ionized [O III]λ5007.

We calculated the mass of the outflowing ionized hydrogen from the measured luminosity of the Hα emission using the following relation (Cresci et al. 2017):

$$M_{\rm ion}^{\rm out} = 3.2 \times 10^5 \left(\frac{L_{\rm broad}(H\alpha)}{10^{40}{\rm erg\ s^{-1}}}\right)\left(\frac{n_e}{100\ {\rm cm^{-3}}}\right)^{-1}. \tag{6}$$

By considering $F_{\rm broad}(H\alpha) = 7.40 \times 10^{-14}$ erg cm^{-2} s^{-1} (integrated flux density over a circular aperture of radius 0.″4 on the extinction corrected outflowing component of Hα line image from GMOS), and mean electron density, $n_e = 1700\ {\rm cm^{-3}}$, we obtained $M^{\rm out}_{\rm ion} \sim 652\,M_\odot$. Using a σ of 123 km s^{-1} (median σ of outflowing component of [O III] λ5007 line), we calculated the kinetic energy of this ionized mass as $E_{\rm KE} = M_{\rm ion}^{\rm out}\langle\sigma^2\rangle = 1.97 \times 10^{50}$ erg. Taking a velocity of 9 km s^{-1} (median of velocity shift of outflowing component of [O III]λ5007 line) and the projected distance of the tip of the eastern jet as 0.″3 (6.3 pc), the time required to reach the terminal point is 2.16×10^{13} s. The power of the outflow is thus $P_{\rm out} = E_{\rm KE}/t = 9.14 \times 10^{36}$ erg s^{-1}.

We calculated the mass and radius of the NLR using the following relations (Peterson 1997):

$$M_{\rm NLR} = 7 \times 10^5 \left(\frac{L({\rm H}\beta)}{10^{41}{\rm erg\ s^{-1}}}\right)\left(\frac{10^3{\rm cm^{-3}}}{n_e}\right) M_\odot, \tag{7}$$

$$R_{\rm NLR} = 19 \left(\frac{L({\rm H}\beta)}{\epsilon 10^{41}{\rm erg\ s^{-1}}}\right)^{1/3}\left(\frac{10^3{\rm cm^{-3}}}{n_e}\right)^{2/3} {\rm pc}. \tag{8}$$

By considering the n_e of 1700 cm^{-3} (obtained from GMOS observations, see Figure 5) and assuming a filling factor (ϵ) of 10^{-2} (typical upper limit; Peterson 1997) we obtained the mass and radius of the NLR of NGC 4395 as 282 $M_\odot$ and 5.35 pc, respectively, over a circular region of 0.″4 radius.

We calculated the bolometric luminosity ($L_{\rm bol}$) using the observed brightness in soft X-ray, hard X-ray, and Hα. In the hard X-ray band (14–195 keV), using the logarithm of the observed luminosity of 40.797 (Liu et al. 2014), we obtained $L_{\rm bol} = 4.97 \times 10^{41}$ erg s^{-1} using the following relation (Ichikawa et al. 2017):

$$\log(L_{\rm bol}) = 0.0378 \times (\log(L_{\rm X}))^2 - 2.03 \times \log(L_{\rm X}) + 61.6. \tag{9}$$

In the soft X-ray band (2–10 keV) using the logarithm of the observed luminosity of 40.3 (Nardini & Risaliti 2011), we obtained an $L_{\rm bol}$ of 1.95×10^{41} erg s^{-1} using the relation given below:

$$\log(L_{\rm bol}) = 0.0378 \times \log(L_{2-10})^2 - 2.00 \times \log(L_{2-10}) + 60.5. \tag{10}$$

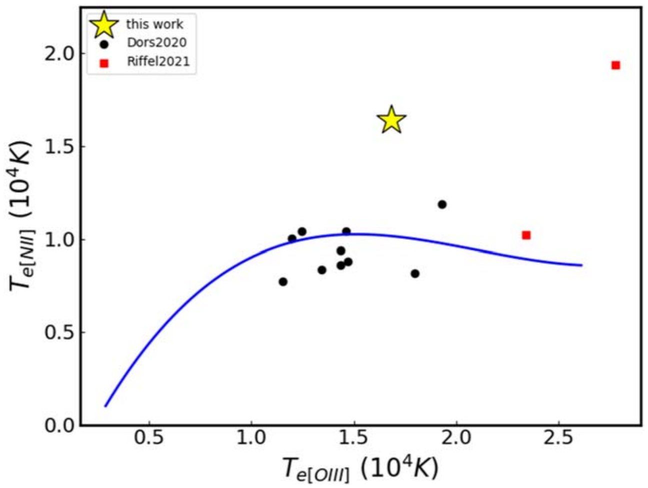

Figure 15. Temperature plot. Here, the yellow point refers to NGC 4395. The blue curve is the AGN photoionization grid. The black and red points are from Dors et al. (2020) and Riffel et al. (2021), respectively.

Similarly, from Hα GMOS observations (considering a circular aperture of 0.4″) using a Hα luminosity of 5.43×10^{38}erg s^{-1}, we obtained $L_{\rm bol} = 3.64 \times 10^{41}$ erg s^{-1} using the equation given below (Greene & Ho 2007):

$$L_{\rm bol} = 2.34 \times 10^{44} \times (L_{{\rm H}\alpha}/10^{42}{\rm erg\ s^{-1}})^{0.86} \tag{11}$$

Thus, from optical and X-ray observations, we found the source to have a bolometric luminosity in the range of (1.95–4.97) × 10^{41} erg s^{-1}.

The disk accretion rate is generally represented by the Eddington ratio ($\lambda_{\rm Edd}$) and is defined as

$$\lambda_{\rm Edd} = L_{\rm bol}/L_{\rm Edd}. \tag{12}$$

Here, $L_{\rm Edd}$ is the Eddington luminosity defined as

$$L_{\rm Edd} = 1.26 \times 10^{38}\left(\frac{M_{\rm BH}}{M_\odot}\right) {\rm erg\ s^{-1}}. \tag{13}$$

Using $L_{\rm bol}$ of (1.95−4.97) × 10^{41} erg s^{-1} and $M_{\rm BH}$ values of (9.1×10^3–3.6×10^5) $M_\odot$ (Peterson et al. 2005; Woo et al. 2019), we obtained $\lambda_{\rm Edd}$ values of 0.004–0.044.

Given the jet power and the bolometric luminosity to be larger than the power of the outflowing ionized emission, the outflow seen in this source on the scale of the NLR of the source could be because of either jet-mode or radiative mode process. The optical spectrum from MaNGA for the central region encompassing the complete core−jet structure having an angular size of 0.″5, shows the presence of the [O III]λ4363 and He II λ4686 lines (see Figure 7). The logarithm of the ratio between the [O III]λ4363 and [O III]λ5007 lines is −1.6; the He II λ4686 and Hβ ratio is −0.72 and the [O III]λ5007 and Hβ ratio is 0.86. These line ratios point to the presence of shocks (Comerford et al. 2017; Moy & Rocca-Volmerange 2002).

A comparison of the emission line ratios obtained from photoionization and shock modeling and observed line ratios also indicates the gas in the central regions of NGC 4395 to be ionized by shocks (see Figure 13). Assuming a spectral index (α) of −0.64 (Yang et al. 2022) for the eastern jet component we derived the Mach number $\left(M_s = \sqrt{\frac{2\alpha - 3}{2\alpha + 1}}\right)$ (Al Yazeedi et al. 2021) of the shock as $M_s = 3.91$. In the line ratios diagnostic diagrams, such as the [O III]λ5007/Hβ versus [S II] λ6717,6731/Hα and [O III]λ5007/Hβ versus [N II]λ6584/Hα diagrams, though all the spaxels lie in the region occupied by

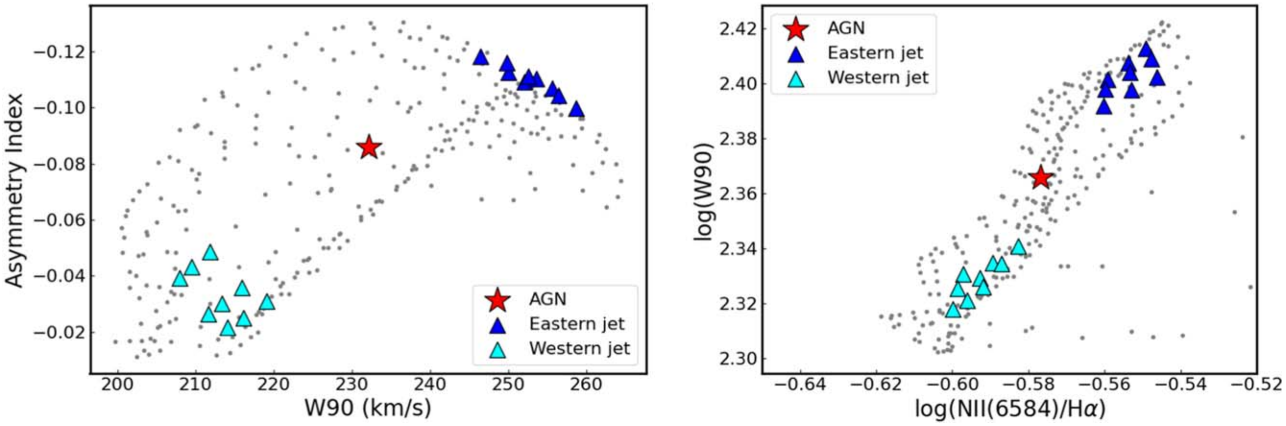

Figure 16. Left panel: distribution of spaxels belonging to the $1'' \times 1''$ region of NGC 4395 in the asymmetry index vs. the velocity dispersion plane. Right panel: distribution of spaxels belonging to the $1'' \times 1''$ region in the W90 ([O III]λ5007 line) vs. the intensity ratio of the [N II]λ6584 and Hα lines.

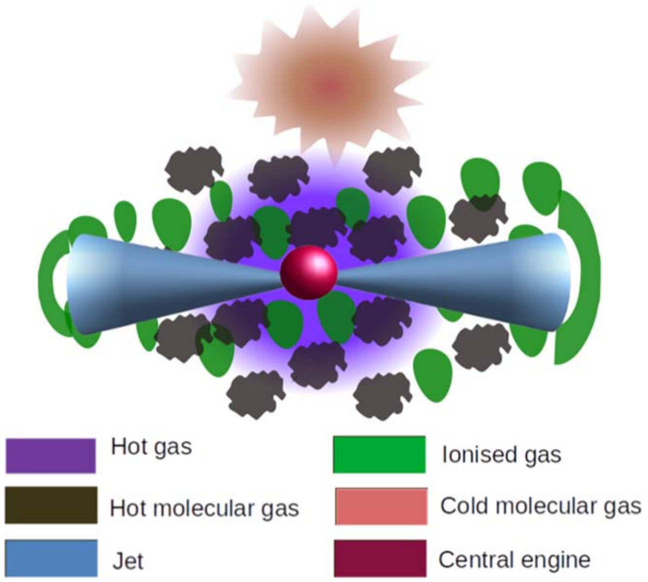

Figure 17. Schematic diagram of our proposed scenario in the inner region of NGC 4395. The jet during its travels outward from the central radio core, interacts with the medium and ionizes the gas via shock excitation. The radio core coincides with the optical Gaia position, the peak of the [O III] emission, and the peak of the 237 GHz emission. Ionized [O III] has a cone-like structure, with the radio jet along the axis and causing the outflows. The CO(2−1) gas is located northward by $\sim 1''$ from the radio core. While ionized [O III]λ5007, warm molecular H2λ2.4085 emissions are along the jet, there is a lack of cold CO in the vicinity, which is possibly due to interactions with the radio jet. As cold gas is needed for the SF process, the lack of cold gas naturally leads to conditions less favorable for SF at scales of ∼10 pc close to the center of NGC 4395.

AGN, the structure is clearly delineated (see Figure 12). Also, in the asymmetry of the line versus the velocity dispersion diagram (see Figure 16; left panel), the spaxels in the eastern jet, occupy a region of higher line asymmetry and higher velocity dispersion, while the western jet occupies a region of lower asymmetry index and lower velocity dispersion. High-velocity dispersion and high asymmetry of the lines are attributed to shock excitation (D'Agostino et al. 2019a). The eastern jet thus seems to occupy a region that is dominated by shock excitation, while the western jet seems to occupy a region of weaker shocks. Spaxels in the central $1'' \times 1''$ region show a tight correlation between the velocity dispersion and the shock-sensitive line ratio [N II]/Hα (see Figure 16, right panel) (Ho et al. 2014). Shock models predict an increase in [N II]/Hα with an increase in shock velocity (Annibali et al. 2010). We show in Figure 15 the position of NGC 4395 in the $T_{\mathrm{e[N\,II]}}$ versus $T_{\mathrm{e[O\,III]}}$ diagram estimated from the MaNGA spectrum. In the same diagram, there are measurements for a few AGN along with predictions from AGN photoionization from `MAPPINGS III`. AGN NGC 4395 lies in a distinct position in this figure, significantly deviant (inclusive of errors in the temperature measurement) from the position occupied by sources photoionized by AGN, pointing to such high temperatures being produced by shocks.

Photoionization and shock modeling from `MAPPINGS III` (Sutherland et al. 2013), the electron temperature distribution, and disturbed kinematics point to the gas in the central region of NGC 4935, excited by shocks. From a multitude of arguments, we conclude that shocks are the dominant process contributing to the excitation of the gas, and such shocks could be due to the interaction of the jet with the ISM in the central 10 pc region of NGC 4395.

3.8. A Radio Jet–ISM Interaction on 10 pc Scale in NGC 4395

From an analysis of data in the optical, infrared, radio, and submillimeter bands, we have found evidence of a low-luminosity jet interacting with its host on the scale of about 10 pc. The eastern jet component, which is brighter in the radio band, is resolved in the high-resolution High Sensitive Array image into two components oriented approximately in the north–south direction, which is nearly orthogonal to the source axis (Wrobel & Ho 2006). This indicates the interaction of the jet plasma with the ISM, with the plasma following the path of least resistance. On the eastern side, the [O III]λ5007 line-emitting gas has higher velocity, higher velocity dispersion, and higher asymmetry (see Figure 16, left panel), possibly due to the shocks associated with the interaction of the radio plasma with the [O III]λ5007 gas. The weakness of the [O III]λ5007 emission can either be due to the gas being more ionized or larger extinction, $E(B-V)$ (see Figure 5) or a combination of both. The weaker jet on the western side has a smaller effect on the [O III]λ5007 gas with a lower velocity dispersion and asymmetry. This suggests that there may be an intrinsic asymmetry in the oppositely directed jets. The radio emission is found to exist co-spatially with the emission at other wavelengths such as the hot ionized [O III]λ5007 emission in

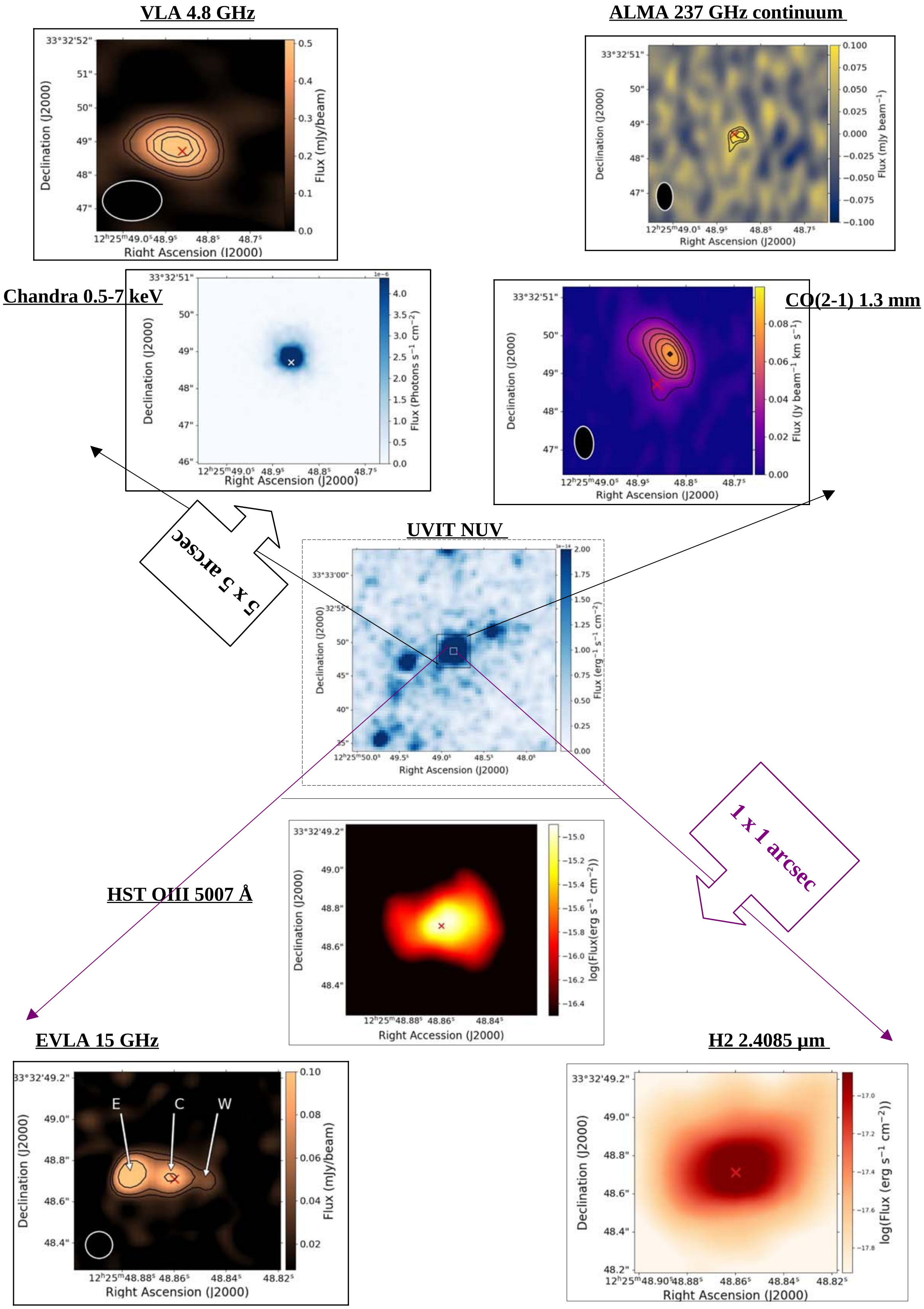

Figure 18. A comprehensive picture of the jet−ISM interaction in the central ∼10 pc region of NGC 4395. In the center is the image of NGC 4395 in the near-UV filter observed with UVIT (Nandi et al. 2023). This image has a size of 30″ × 30″. Also, shown in the same image are two square boxes one of size 5″ × 5″ (black color) and the other of 1″ × 1″ (white color). On the top panels are the 4.8 GHz image from the VLA, the 237 GHz image from ALMA, the CO(2-1) image from ALMA, and the X-ray image in the 0.5–7 keV from Chandra. These images have a size of 5″ × 5″. The bottom panels show the 15 GHz image from the VLA, the molecular H2λ2.4085 image from Gemini, and the [O III]λ5007 image from HST over a 1″ × 1″ region. In each of these images, the core of NGC 4395 taken as the Gaia position, is shown as a cross.

the optical band, the warm molecular $H_2\lambda2.4085$ in the infrared band, and the 237 GHz emission in the submillimeter band. However, the cold CO(2−1) emission is displaced by $\approx 1''$ from the core. The presence of cold molecular gas is conducive to SF. The displacement of the CO(2−1) gas, and the paucity of cold gas along the source axis, possibly due to interactions by the jet, have led to the conditions less favorable for SF on a 10 pc scale. A schematic of our proposed coherent picture of the central region of NGC 4395 is shown in Figure 17.

4. Summary

In this work, we carried out a systematic investigation of the central region of NGC 4395 using imaging and spatially resolved spectroscopic observations. We summarize our main findings below:

1. From VLA images at 15 GHz, NGC 4395 is found to show a triple radio structure having a projected size of ∼10 pc. The central component of the triple structure is found to coincide with the optical Gaia position, which we call the radio core. The source is also highly asymmetric in brightness with the eastern component brighter than the western one.
2. The triple radio structure in NGC 4395 is reminiscent of bipolar jet ejection in radio-loud AGN and the eastern and western components of this triple structure are formed by the low-power jet ($P_{\rm jet} = (1.3 \pm 0.3) \times 10^{40}$ erg s^{-1}) powered by the intermediate-mass black hole in NGC 4395.
3. From HST observations we found the [O III]λ5007 emission to be prevalent over the entire extent of the radio emission with the peak of the [O III]λ5007 emission coinciding with the optical Gaia position and the radio core. The [O III]λ5007 emission is asymmetric and shows a convex-shaped structure at the terminal points on either side of the core of NGC 4395 indicating an outflow. This asymmetry in the brightness of [O III]λ5007 emission could be due to intrinsic asymmetries causing different levels of ionization or differences in the degree of extinction or a combination of both.
4. The X-ray emission in the 0.5−7 keV band is found to overlap with the radio jet. Similarly, the peak of the continuum emission at 237 GHz is spatially coincident with the radio core. Also, the molecular $H_2\lambda2.4085$ is found to be extended along the radio jet direction and has a close correspondence with the radio emission.
5. From AGN photoionization and shock modeling from `MAPPINGS III` and the distribution of the electron temperature distribution, we conclude that the gas in the central region of NGC 4395 is excited mostly by shocks and such shocks could be due to the interaction of the radio jet with the ISM in the central parsec region of NGC 4395. This is the first detection of radio jet–ISM interaction at such small spatial scales.
6. The cold CO(2−1) emission is found to be displaced northward of the radio core by about $1''$ (∼20 pc). The paucity of cold molecular gas in the central region, possibly due to interactions with the jet makes conditions less favorable for SF on scales of about 10 pc in NGC 4395.

The detections of AGN and intermediate-mass black holes in a number of dwarf galaxies in recent years have opened the possibility of studying feedback processes in dwarf galaxies. Studies of nearby dwarfs also enable us to probe feedback processes on parsec scales. Schutte & Reines (2022) reported a 150 pc long ionized filament in the dwarf galaxy Henize 2–10 from HST observations, which connect the black hole region with a site of recent SF. Nyland et al. (2017) reported possible evidence of shock excitation in the nearby dwarf AGN galaxy NGC 404 with an amorphous radio outflow extending over ∼17 pc. NGC 4395 is the clearest example of a dwarf AGN with a triple radio structure, where there is clear evidence of jet −ISM interaction on the smallest scale of ∼5 pc on either side of the core. A comprehensive picture depicting this jet−ISM interaction in the central parsec-scale region based on the analysis of images from multiple wavelengths is shown in Figure 18. This finding will bolster the prospect of finding more such instances in dwarf AGN host galaxies, paving the way for a better understanding of the complex interplay between AGN and their hosts on such small scales in these galaxies.

Acknowledgments

We acknowledge the reviewer for his/her insightful comments, which helped to improve the quality of the manuscript. This research has made use of data obtained from the Chandra Data Archive and the Chandra Source Catalog and software provided by the Chandra X-ray Center (CXC) in the application packages CIAO and Sherpa. Based on observations made with the NASA/ESA Hubble Space Telescope, and obtained from the Hubble Legacy Archive, which is a collaboration between the Space Telescope Science Institute (STScI/NASA), the Space Telescope European Coordinating Facility (ST-ECF/ESAC/ESA) and the Canadian Astronomy Data Center (CADC/NRC/CSA). This publication uses data from MaNGA (Mapping Nearby Galaxies at APO) survey, which is one of the programs of the Sloan Digital Sky Survey (SDSS) IV. Funding for the Sloan Digital Sky Survey IV has been provided by the Alfred P. Sloan Foundation, the U.S. Department of Energy Office of Science, and the Participating Institutions.

SDSS-IV acknowledges support and resources from the Center for High Performance Computing at the University of Utah. The SDSS website is at www.sdss4.org.

SDSS-IV is managed by the Astrophysical Research Consortium for the Participating Institutions of the SDSS Collaboration including the Brazilian Participation Group, the Carnegie Institution for Science, Carnegie Mellon University, Center for Astrophysics | Harvard & Smithsonian, the Chilean Participation Group, the French Participation Group, Instituto de Astrofísica de Canarias, The Johns Hopkins University, Kavli Institute for the Physics and Mathematics of the Universe (IPMU)/University of Tokyo, the Korean Participation Group, Lawrence Berkeley National Laboratory, Leibniz Institut für Astrophysik Potsdam (AIP), Max-Planck-Institut für Astronomie (MPIA Heidelberg), Max-Planck-Institut für Astrophysik (MPA Garching), Max-Planck-Institut für Extraterrestrische Physik (MPE), National Astronomical Observatories of China, New Mexico State University, New York University, University of Notre Dame, Observatário Nacional/MCTI, The Ohio State University, Pennsylvania State University, Shanghai Astronomical Observatory, United Kingdom Participation Group, Universidad Nacional

Autónoma de México, University of Arizona, University of Colorado Boulder, University of Oxford, University of Portsmouth, University of Utah, University of Virginia, University of Washington, University of Wisconsin, Vanderbilt University, and Yale University.

This work is partly based on observations obtained at the Gemini Observatory, which is operated by the Association of Universities for Research in Astronomy, Inc., under a cooperative agreement with the NSF on behalf of the Gemini partnership: the National Science Foundation (United States), the Science and Technology Facilities Council (United Kingdom), the National Research Council (Canada), CONICYT (Chile), the Australian Research Council (Australia), Ministério da Ciênciae Tecnologia (Brazil) and southeast CYT (Argentina). This paper makes use of the following ALMA data: ADS/JAO.ALMA#2017.1.00572.S. ALMA is a partnership of ESO (representing its member states), NSF (USA) and NINS (Japan), together with NRC (Canada), MOST and ASIAA (Taiwan), and KASI (Republic of Korea), in cooperation with the Republic of Chile. The Joint ALMA Observatory is operated by ESO, AUI/NRAO and NAOJ. This publication uses radio observations carried out using the National Radio Astronomy Observatory facilities Very Large Array (VLA) and Karl G. Jansky Very Large Array (JVLA). The National Radio Astronomy Observatory is a facility of the National Science Foundation operated under cooperative agreement by Associated Univerties, Inc. This work has made use of the NASA Astrophysics Data System (ADS) and the NASA/IPAC extragalactic database (NED).[12] This work has made use of data from the European Space Agency (ESA) mission Gaia (https://www.cosmos.esa.int/gaia), processed by the Gaia Data Processing and Analysis Consortium (DPAC, https://www.cosmos.esa.int/web/gaia/dpac/consortium). Funding for the DPAC has been provided by national institutions, in particular, the institutions participating in the Gaia Multilateral Agreement. The authors acknowledge Dr. Jarle Brinchmann for sharing the library of the `ITERA` code. A few of the authors thank the Alexander von Humboldt Foundation, Germany, for the award of the Group Linkage long-term research program. P.N. thanks the Council of Scientific and Industrial Research (CSIR), Government of India, for supporting her research under the CSIR Junior/Senior research fellowship program through grant No. 09/079(2867)/2021-EMR-I.

Software: IRAF (Tody 1986), Astropy (Astropy Collaboration et al. 2013, 2018, 2022), `SciPy` (Virtanen et al. 2020), `NumPy` (Harris et al. 2020), `Matplotlib` (Hunter 2007), `PyNeb` (Luridiana et al. 2015), `AIPS` (Wells 1985), `CASA` (McMullin et al. 2007; CASA Team et al. 2022), `Chandra` (Fruscione et al. 2006), `MAPPINGS III` (Sutherland et al. 2013).

ORCID iDs

Payel Nandi https://orcid.org/0009-0003-9765-3517
C. S. Stalin https://orcid.org/0000-0002-4998-1861
D. J. Saikia https://orcid.org/0000-0002-4464-8023
Rogemar A. Riffel https://orcid.org/0000-0003-0483-3723
Arijit Manna https://orcid.org/0000-0001-9133-3465
Sabyasachi Pal https://orcid.org/0000-0003-2325-8509
Dominika Wylezalek https://orcid.org/0000-0003-2212-6045
Vaidehi S. Paliya https://orcid.org/0000-0001-7774-5308
Payaswini Saikia https://orcid.org/0000-0002-5319-6620
Markus-Kissler Patig https://orcid.org/0000-0002-5908-1488
Ram Sagar https://orcid.org/0000-0003-4973-4745

References

Al Yazeedi, A., Katkov, I. Y., Gelfand, J. D., et al. 2021, ApJ, 916, 102
Annibali, F., Bressan, A., Rampazzo, R., et al. 2010, A&A, 519, A40
Astropy Collaboration, Price-Whelan, A. M., Lim, P. L., et al. 2022, ApJ, 935, 167
Astropy Collaboration, Price-Whelan, A. M., Sipőcz, B. M., et al. 2018, AJ, 156, 123
Astropy Collaboration, Robitaille, T. P., Tollerud, T. P., et al. 2013, A&A, 558, A33
Baldwin, J. A., Phillips, M. M., & Terlevich, R. 1981, PASP, 93, 5
Bohn, T., Canalizo, G., Veilleux, S., & Liu, W. 2021, ApJ, 911, 70
Brum, C., Diniz, M. R., Riffel, R. A., et al. 2019, MNRAS, 486, 691
CASA Team, Bean, B., Bhatnagar, S., et al. 2022, PASP, 134, 114501
Cavagnolo, K. W., McNamara, B. R., Nulsen, P. E. J., et al. 2010, ApJ, 720, 1066
Cedrés, B., & Cepa, J. 2002, A&A, 391, 809
Comerford, J. M., Barrows, R. S., Greene, J. E., & Pooley, D. 2017, ApJ, 847, 41
Cresci, G., Vanzi, L., Telles, E., et al. 2017, A&A, 604, A101
D'Agostino, J. J., Kewley, L. J., Groves, B. A., et al. 2019a, MNRAS, 485, L38
D'Agostino, J. J., Kewley, L. J., Groves, B. A., et al. 2019b, MNRAS, 487, 4153
Dors, O. L., Maiolino, R., Cardaci, M. V., et al. 2020, MNRAS, 496, 3209
Fabian, A. C. 2012, ARA&A, 50, 455
Filippenko, A. V., Ho, L. C., & Sargent, W. L. W. 1993, ApJL, 410, L75
Filippenko, A. V., & Sargent, W. L. W. 1989, ApJL, 342, L11
Fruscione, A., McDowell, J. C., Allen, G. E., et al. 2006, Proc. SPIE, 6270, 62701V
García-Bernete, I., Alonso-Herrero, A., García-Burillo, S., et al. 2021, A&A, 645, A21
Greene, J. E., & Ho, L. C. 2007, ApJ, 670, 92
Groves, B., & Allen, M., 2013 ITERA: IDL Tool for Emission-line Ratio Analysis, Astrophysics Source Code Library, ascl:1307.012
Hägele, G. F., Díaz, Á. I., Terlevich, E., et al. 2008, MNRAS, 383, 209
Harris, C. R., Millman, K. J., van der Walt, S. J., et al. 2020, Natur, 585, 357
Ho, I. T., Kewley, L. J., Dopita, M. A., et al. 2014, MNRAS, 444, 3894
Ho, L. C., & Ulvestad, J. S. 2001, ApJS, 133, 77
Hunter, J. D. 2007, CSE, 9, 90
Ichikawa, K., Ricci, C., Ueda, Y., et al. 2017, ApJ, 835, 74
Kaiser, C. R., & Alexander, P. 1999, in ASP Conf. Ser. 176, Observational Cosmology: The Development of Galaxy Systems, ed. G. Giuricin, M. Mezzetti, & P. Salucci (San Francisco, CA: ASP), 377
Kammoun, E. S., Nardini, E., Zoghbi, A., et al. 2019, ApJ, 886, 145
Kauffmann, G., Heckman, T. M., Tremonti, C., et al. 2003, MNRAS, 346, 1055
Kewley, L. J., Heisler, C. A., Dopita, M. A., & Lumsden, S. 2001, ApJS, 132, 37
Kirk, J. G., Guthmann, A. W., Gallant, Y. A., & Achterberg, A. 2000, ApJ, 542, 235
Koudmani, S., Sijacki, D., & Smith, M. C. 2022, MNRAS, 516, 2112
Lal, D. V., Shastri, P., & Gabuzda, D. C. 2011, ApJ, 731, 68
Liu, T., Wang, J. X., Yang, H., Zhu, F. F., & Zhou, Y. Y. 2014, ApJ, 783, 106
Luridiana, V., Morisset, C., & Shaw, R. A. 2015, A&A, 573, A42
Maiolino, R., Gallerani, S., Neri, R., et al. 2012, MNRAS, 425, L66
Maiolino, R., Russell, H. R., Fabian, A. C., et al. 2017, Natur, 544, 202
Manzano-King, C. M., Canalizo, G., & Sales, L. V. 2019, ApJ, 884, 54
McMullin, J. P., Waters, B., Schiebel, D., Young, W., & Golap, K. 2007, in ASP Conf. Ser. 376, Astronomical Data Analysis Software and Systems XVI, ed. R. A. Shaw, F. Hill, & D. J. Bell (San Francisco, CA: ASP), 127
Miller, J. S., & Mathews, W. G. 1972, ApJ, 172, 593
Morganti, R., Oosterloo, T., Tadhunter, C., Bernhard, E. P., & Raymond Oonk, J. B. 2021, A&A, 656, A55
Moy, E., & Rocca-Volmerange, B. 2002, A&A, 383, 46
Mukherjee, D., Bicknell, G. V., Wagner, A. Y., Sutherland, R. S., & Silk, J. 2018, MNRAS, 479, 5544
Nandi, P., Stalin, C. S., Saikia, D. J., et al. 2023, ApJ, 950, 81
Nardini, E., & Risaliti, G. 2011, MNRAS, 417, 2571
Nesvadba, N. P. H., Bicknell, G. V., Mukherjee, D., & Wagner, A. Y. 2020, A&A, 639, L13
Nyland, K., Davis, T. A., Nguyen, D. D., et al. 2017, ApJ, 845, 50
O'Dea, C. P., & Saikia, D. J. 2021, A&ARv, 29, 3
Panessa, F., Baldi, R. D., Laor, A., et al. 2019, NatAs, 3, 387

---

[12] https://ned.ipac.caltech.edu

Peterson, B. M. 1997, An Introduction to Active Galactic Nuclei (Cambridge: Cambridge Univ. Press)

Peterson, B. M., Bentz, M. C., Desroches, L. B., et al. 2005, ApJ, 632, 799

Rampadarath, H., Soria, R., Urquhart, R., et al. 2018, MNRAS, 476, 2876

Rees, M. J. 1984, ARA&A, 22, 471

Riffel, R. A., Dors, O. L., Armah, M., et al. 2021, MNRAS, 501, L54

Roy, A. L., Wilson, A. S., Ulvestad, J. S., & Colbert, J. M. 2000, in EVN Symposium 2000, Proc. of the 5th European VLBI Network Symposium, ed. J. E. Conway et al. (Onsala: Onsala Space Obs.), 7

Rusinek, K., Sikora, M., Kozieł-Wierzbowska, D., & Godfrey, L. 2016, MNRAS, 466, 2294

Saikia, D. J. 2022, JApA, 43, 97

Saikia, D. J., Jeyakumar, S., Mantovani, F., et al. 2003, PASA, 20, 50

Saikia, P., Körding, E., Coppejans, D. L., et al. 2018, A&A, 616, A152

Schutte, Z., & Reines, A. E. 2022, Natur, 601, 329

Shin, J., Woo, J. H., Chung, A., et al. 2019, ApJ, 881, 147

Sutherland, R., Dopita, M., Binette, L., & Groves, B., 2013 MAPPINGS III: Modelling And Prediction in PhotoIonized Nebulae and Gasdynamical Shocks, Astrophysics Source Code Library, ascl:1306.008

Thim, F., Hoessel, J. G., Saha, A., et al. 2004, AJ, 127, 2322

Tody, D. 1986, Proc. SPIE, 627, 733

Vaughan, S., Iwasawa, K., Fabian, A. C., & Hayashida, K. 2005, MNRAS, 356, 524

Veilleux, S., Kim, D. C., Sanders, D. B., Mazzarella, J. M., & Soifer, B. T. 1995, ApJS, 98, 171

Venturi, G., Cresci, G., Marconi, A., et al. 2021, A&A, 648, A17

Véron-Cetty, M. P., & Véron, P. 2006, A&A, 455, 773

Virtanen, P., Gommers, R., Oliphant, T. E., et al. 2020, NatMe, 17, 261

Wells, D. C. 1985, in Data Analysis in Astronomy, ed. V. di Gesu et al. (New York: Plenum), 195

Whittle, M., Silverman, J. D., Rosario, D. J., Wilson, A. S., & Nelson, C. H. 2004, in IAU Symp. 222, The Interplay Among Black Holes, Stars and ISM in Galactic Nuclei, ed. T. Storchi-Bergmann, L. C. Ho, & H. R. Schmitt (Cambridge: Cambridge Univ. Press), 299

Woo, J. H., Cho, H., Gallo, E., et al. 2019, NatAs, 3, 755

Wrobel, J. M., & Ho, L. C. 2006, ApJL, 646, L95

Yang, J., Yang, X., Wrobel, J. M., et al. 2022, MNRAS, 514, 6215

Zakamska, N. L., & Greene, J. E. 2014, MNRAS, 442, 784